Autumn Precipitation Trends over Southern Hemisphere Midlatitudes as Simulated by CMIP5 Models

Ariaan Purich and Tim Cowan

CSIRO Marine and Atmospheric Research, CSIRO Water for a Healthy Country Flagship, CSIRO Wealth from Oceans Flagship, Aspendale, Victoria, Australia

Seung-Ki Min

School of Environmental Science and Engineering, Pohang University of Science and Technology, Pohang, Gyungbuk, South Korea

Wenju Cai

CSIRO Marine and Atmospheric Research, CSIRO Water for a Healthy Country Flagship, CSIRO Wealth from Oceans Flagship, Aspendale, Victoria, Australia

(Manuscript received 18 December 2012, in final form 22 March 2013)

ABSTRACT

In recent decades, Southern Hemisphere midlatitude regions such as southern Africa, southeastern Australia, and southern Chile have experienced a reduction in austral autumn precipitation; the cause of which is poorly understood. This study focuses on the ability of global climate models that form part of the Coupled Model Intercomparison Project phase 5 to simulate these trends, their relationship with extratropical and subtropical processes, and implications for future precipitation changes. Models underestimate both the historical autumn poleward expansion of the subtropical dry zone and the positive southern annular mode (SAM) trend. The multimodel ensemble (MME) is also unable to capture the spatial pattern of observed precipitation trends across semiarid midlatitude regions. However, in temperate regions that are located farther poleward such as southern Chile, the MME simulates observed precipitation declines. The MME shows a strong consensus in twenty-first-century declines in autumn precipitation across southern Chile in both the medium–low and high representative concentration pathway (RCP) scenarios and across southern Africa in the high RCP scenario, but little change across southeastern Australia. Projecting a strong positive SAM trend and continued subtropical dry-zone expansion, the models converge on large SAM and dry-zone-expansion-induced precipitation declines across southern midlatitudes. In these regions, the strength of future precipitation trends is proportional to the strength of modeled trends in these phenomena, suggesting that unabated greenhouse gas–induced climate change will have a large impact on austral autumn precipitation in such midlatitude regions.

1. Introduction

Over the latter part of the twentieth century and the first decade of the twenty-first century, midlatitude regions of the Southern Hemisphere (SH) have experienced a marked drying trend during austral autumn (March–May) (e.g., Cai and Cowan 2008a; Nicholls 2010; Cai et al. 2012). While the cause of this precipitation decline is not well understood, it has been suggested that the expanding tropics (e.g., Seidel et al. 2008; Johanson and Fu 2009; Cai et al. 2012) and a poleward shift in extratropical weather systems (e.g., Thompson and Solomon 2002; Fyfe 2003; Cai and Cowan 2013) might play a role in driving these trends.

Since the late 1970s the tropics have expanded poleward in all seasons, with the strongest SH trends of around 2°–4.5° being observed during autumn (Hu and Fu 2007; Hu et al. 2011), although the impact on regional SH midlatitude rainfall has not been uniform (Cai et al. 2012). The subtropical ridge has been used as an indicator of the descending branch of the Hadley circulation in studies of subtropical dry-zone expansion

Corresponding author address: Ariaan Purich, CSIRO Marine and Atmospheric Research, PMB 1, Aspendale VIC 3195, Australia.
E-mail: ariaan.purich@csiro.au

(e.g., Timbal and Drosdowsky 2013). Whereas poleward shifts in the edge of the Hadley cell have been detected in streamfunction-based metrics (e.g., Johanson and Fu 2009), a discernible shift in the subtropical ridge in the eastern Australian region has not been detected (Drosdowsky 2005). The reasons for this apparent discrepancy are not known; however, a strengthening of the subtropical ridge has been observed and has been linked with the autumn–spring rainfall decline in southeastern Australia (Timbal and Drosdowsky 2013).

The poleward expansion of the tropical belt and subtropical dry zone are consistent with a poleward shift in the storm tracks and westerly wind belt (e.g., Yin 2005), associated with recent trends toward the positive polarity of the southern annular mode (SAM), the dominant mode of atmospheric variability in the extratropical SH (Thompson and Wallace 2000). In recent decades the SAM has exhibited pronounced tropospheric trends toward its positive phase during austral summer and autumn in various fields (e.g., sea level pressure, 500-hPa geopotential height, surface temperature, and zonal wind) (Thompson and Solomon 2002; Marshall 2003). The associated wind changes have induced an intensification and poleward shift of the oceanic gyre circulations (Cai and Cowan 2007) and a poleward shift in the extratropical eddy-driven westerly jet and associated storm tracks (Frederiksen and Frederiksen 2007). The trend is consistent with circulation changes associated with both a decrease in stratospheric ozone and an increase in greenhouse gases (Shindell and Schmidt 2004; Arblaster and Meehl 2006; Son et al. 2010), although ozone depletion is thought to dominate SH surface climate changes only during austral summer (Perlwitz et al. 2008; Son et al. 2009; Polvani et al. 2011).

Observed variability in the SAM has been linked with variability in precipitation over southern Africa (Reason and Rouault 2005), southwestern and southeastern Australia (Hendon et al. 2007; Meneghini et al. 2008; Murphy and Timbal 2008; Risbey et al. 2009; Cai et al. 2011), New Zealand (Kidston et al. 2009; Purdie et al. 2011), and southern South America (Silvestri and Vera 2003; Haylock et al. 2006). Observed decreases in annual-mean precipitation linked to the positive tendency of the SAM are centered around 45°S and are associated with increased geopotential height, subsidence, and reduced cloudiness (Gillett et al. 2006).

The simulation of the subtropical dry-zone expansion and SAM trends by coupled climate models has been the focus of many detection and attribution studies. Such studies have made use of the wide range of model output available through phase 3 of the Coupled Model Intercomparison Project (CMIP3). For example, the widening of the Hadley cell in response to increasing greenhouse gas concentrations and stratospheric ozone depletion was found to be replicated in the CMIP3 twentieth-century simulations; however, the widening was significantly smaller than that observed (Johanson and Fu 2009). In the extratropics, the CMIP3 models showed better skill in capturing the positive SAM trends in austral summer (Fogt et al. 2009), with ozone depletion attributed as the dominant mechanism driving these trends (e.g., Miller et al. 2006; Cai and Cowan 2007). The most significant trends in the observed SAM index occur during austral autumn (over 1957–2005; Fogt et al. 2009); however, CMIP3 models tend to simulate weak autumn SAM trends, differing largely from the observations. Based on SAM variability analysis from reconstructions, Fogt et al. (2009) concluded that the observed autumn trend in the SAM was primarily a result of natural climate variability, with anthropogenic forcing contributing to a lesser portion of the trend.

The annual relationship between the SAM and precipitation variability in the CMIP3 models has also been investigated: the models capture the observed negative relationship in the 35°–50°S latitude band over regions such as New Zealand and southern Chile, and the observed positive relationship in the regions farther north such as southern Africa and southern Australia (Karpechko et al. 2009). However, they fail to capture the observed negative relationship in southeastern South America (La Plata basin region) (Karpechko et al. 2009).

With the recent availability of the next generation of global climate models from phase 5 of the Coupled Model Intercomparison Project (CMIP5), we assess the ability of these models to capture the observed trends in austral autumn precipitation across the SH midlatitude regions. This season is chosen because it is when many midlatitude regions exhibit their largest precipitation trends (Fig. 1a; other seasons not shown), and because such trends can have important implications for water resource management annually. For example, Cai and Cowan (2008b) showed that for southeastern Australia, autumn rainfall plays an important role in wetting the soil and preparing catchments for runoff generation during austral winter and spring; declines in autumn rainfall have thus had significant impacts on annual streamflow in the Murray-Darling basin. The dynamics of what has driven recent declines, however, still remain poorly understood (Murphy and Timbal 2008); a poleward shift of the subtropical dry zone has been offered as one explanation for southeastern Australia (Cai et al. 2012). How well CMIP5 models simulate
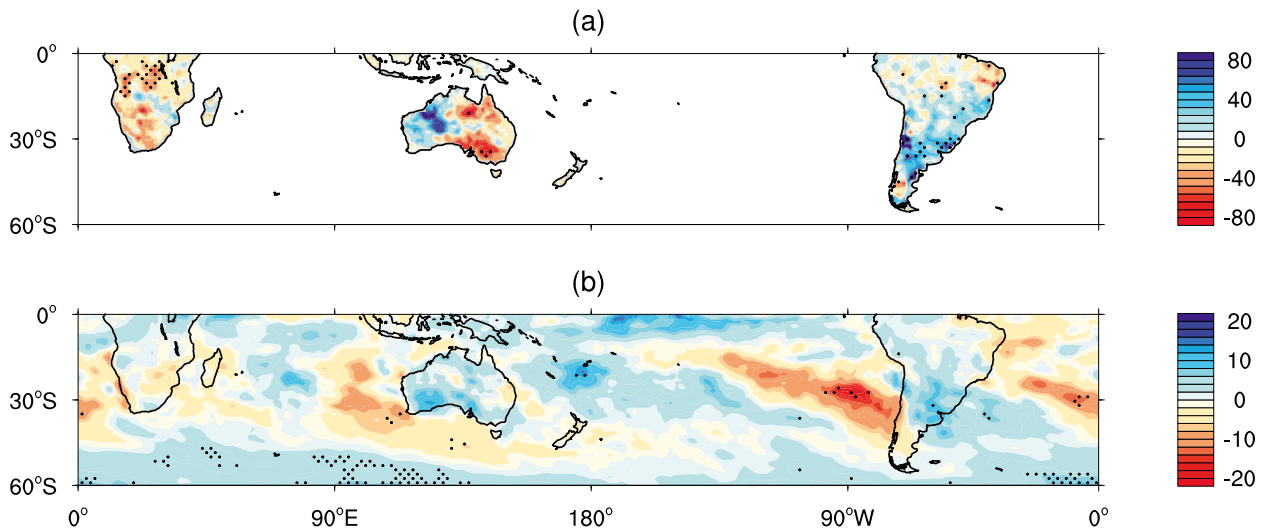
FIG. 1. Austral autumn trends in precipitation over 1961–2005: (a) GPCC precipitation and (b) CMIP5 historical MME. Trends are expressed as a percentage change of climatology per 45 years and note that the two color bars have different limits. Stippling in (a) indicates that the observed trend is significant at the 95% confidence level as determined by a two-sided Student's t test and in (b) where ≥80% of the 34 models agree on the sign of the ensemble-mean trend.

the recent subtropical dry-zone expansion and positive trends in the SAM during austral autumn, what changes are projected into the future, and the impact on precipitation across the SH midlatitude regions are investigated.

2. Data and methods

In investigating factors responsible for trends in precipitation we make use of monthly observations and CMIP5 climate model data, averaged over austral autumn. The historical analysis period is 1961–2005, chosen to capture the periods of strongest precipitation changes (Cai et al. 2012) and to make a fair comparison to the climate model simulations. The future analysis period is 2006–50, chosen for continuity and to match the historical period in length. Linear trends in autumn precipitation, the SAM index, and the SH Hadley cell edge (HCE; subtropical dry zone) are calculated over these periods.

In our analysis, the SAM is calculated using empirical orthogonal function (EOF) analysis so that variations in the spatial patterns among different models are accounted for. The SAM index is defined as the principal component time series of the first EOF of mean sea level pressure (MSLP) from 20° to 90°S. To test sensitivity to the SAM definition, two alternate indices are also investigated: the difference between zonal-mean MSLP at 40° and 65°S [a nonnormalized version of the Gong and Wang (1999) definition] and the difference between

normalized proxy zonal-mean MSLP estimated from six locations at approximately 40°S and six locations at approximately 65°S, as described by Marshall (2003). Results obtained using all three SAM definitions are very similar (not shown), indicating that they are not sensitive to the choice of SAM index definition. Hereafter, the SAM index refers to the first EOF of MSLP, unless specified otherwise.

The HCE is calculated using the meridional mass streamfunction definition (as in Johanson and Fu 2009), with the position described as the subtropical latitude where the meridional mass streamfunction at 500 hPa becomes zero (~30°–40°S). This definition has been extensively used in observational and modeling studies (Hu and Fu 2007; Son et al. 2009; Hu et al. 2011; Cai et al. 2012; Min and Son 2013). The subtropical ridge is not used as a measure of HCE here, as it is regionally defined (Timbal and Drosdowsky 2013), whereas the streamfunction definition encompasses the entire hemisphere.

Precipitation observations gridded at a resolution of 0.5° × 0.5° are utilized from the Global Precipitation Climatology Centre (GPCC) version 6 monthly precipitation dataset (Beck et al. 2005). This dataset is chosen because, although it only contains land surface precipitation data, it is based on in situ rain gauge data interpolated on to a grid, and is available over the full period of analysis. Statistical significance of observed trends is determined using a two-sided Student's t test. Results are similar when other station-based gridded

precipitation datasets are used,[1] as per Cai et al. (2012). Satellite- and observation-based land and ocean precipitation data over 1979–2005 from the Global Precipitation Climatology Project (GPCP) version 2 dataset (Adler et al. 2003) and from the Climate Prediction Center (CPC) Merged Analysis of Precipitation (CMAP) dataset (Xie and Arkin 1997) are used to assess trends over the oceans, albeit over a shorter time scale.

To calculate the observational SAM index, based on the period of interest (1961–2005), MSLP is taken from the National Centers for Environmental Prediction–National Center for Atmospheric Research reanalysis (NNR) (Kalnay et al. 1996) and bilinearly interpolated to a $1° \times 1°$ grid. However, it is known that spurious trends exist in NNR over the SH high latitudes (Marshall 2003): to correct for this, prior to EOF analysis, we regress the linearly detrended NNR MSLP ($MSLP|_{dt}$) onto the linearly detrended Marshall (2003) observational station-based SAM index ($station|_{dt}$) to obtain a regression equation between MSLP and the station-based SAM index at each grid point (reg-equn):

$$\text{reg-equn}(x, y) = \text{regression}[\text{station}|_{dt}(t), MSLP|_{dt}(x, y, t)], \quad (1)$$

where

$$\text{reg-equn}(x, y) = \text{slope}(x, y) + y\text{-int}(x, y). \quad (2)$$

We then multiply the regression slope field by the SAM index (containing the trend; station) to obtain a corrected MSLP dataset ($MSLP|_{corr}$):

$$MSLP|_{corr}(x, y, t) = [\text{slope}(x, y) \times \text{station}(t)] \\ + y\text{-int}(x, y), \quad (3)$$

which is used in all further analysis.

For consistency, the observed HCE is also calculated from NNR meridional winds. For comparison, the National Oceanic and Atmospheric Administration–Cooperative Institute for Research in Environmental Sciences Twentieth Century Reanalysis (20CR) version 2 (Compo et al. 2011) is also used. Both SAM and HCE time series are calculated in the same manner as for NNR. 20CR results are only shown in Figs. 2 and 4 and are referred to only when there are notable differences from NNR.

---

[1] Climate Prediction Center global land precipitation, University of East Anglia Climatic Research Unit precipitation (version 3.1) and University of Delaware interpolated precipitation (version 3.01).

We utilize model output of precipitation, MSLP, and meridional wind from the CMIP5 historical experiment (34 models; see Table 1, which provides all expansions) and the representative concentration pathway (RCP) 4.5 (medium–low global anthropogenic radiative forcing scenario; 16 models) and 8.5 (high global anthropogenic radiative forcing scenario; 21 models) experiments (Taylor et al. 2012). For each model and experiment, the first simulation (r1i1p1) is used in analysis.

All precipitation and MSLP datasets are first bilinearly interpolated to a standard $1° \times 1°$ grid. Trends are calculated for each model individually and multimodel ensemble (MME) trends for each experiment are then calculated by averaging the trends of each model equally (Figs. 1b and 6b and 6c). The intermodel relationship between precipitation trends and SAM (HCE) trends is analyzed by calculating the correlation coefficient between all model trends at each grid point, with statistical significance determined using a two-sided Student's t test (Figs. 3 and 6d and 6e). The SAM-congruent precipitation trend [$\text{pr-trend}|_{SAM}(x, y)$] is determined for each model by calculating the regression coefficient between the linearly detrended SAM index [$SAM|_{dt}(t)$] and the linearly detrended precipitation [$pr|_{dt}(x, y, t)$] at each grid point and multiplying by the SAM trend (SAM-trend),

$$\text{pr-trend}|_{SAM}(x, y) \\ = \text{regression}[SAM|_{dt}(t), pr|_{dt}(x, y, t)] \times \text{SAM-trend}, \quad (4)$$

and then averaging across all models (Fig. 5b). The same procedure is carried out for precipitation trends congruent with the HCE trend (Fig. 5d).

3. Results

a. Observed and modeled precipitation trends

The observed trends in SH austral autumn precipitation, expressed as a percentage change in climatology per 45 years, are shown in Fig. 1a. A decreasing trend is seen across many of the midlatitude regions: southern Africa, southeastern Australia, southern New Zealand, and southern Chile. In contrast, an increasing trend in precipitation is seen across much of western Australia and southeastern South America.

Observed trends in precipitation over the ocean are not available for the full time period analyzed here. Trends over 1979–2005 from CMAP and GPCP (not shown) are somewhat inconsistent over the southern and midlatitude oceans. CMAP shows a strong dipole pattern in the trends with increased precipitation at

~60°S and decreased precipitation at ~45°S: these trends are much less pronounced in the GPCP. Previous studies have found inconsistencies between CMAP and GPCP in detecting changes in ocean precipitation (e.g., Zhou et al. 2008), likely due to the different algorithms used to retrieve rainfall from satellite measurements (Gruber et al. 2000). The disagreement between these two observational products, along with the limited time period over which analysis is possible, makes assessment of model performance over the oceans difficult.

To a large degree, many of the observed midlatitude trends are not captured by the CMIP5 MME (Fig. 1b). Except in a very small part of southeastern South America, across no landmass region do at least 80% of the models agree on the sign of the ensemble-mean trend (as indicated by stippling). The magnitude of trends in the MME is also much less than that of the observations over all regions, in part due to the high intermodel variation exhibited in the trend spatial patterns and the nature of multimodel averaging.

Comparing Figs. 1a and 1b, the models fail to capture and in fact show opposite trends (increasing precipitation) over the southeastern tip of Africa and southeastern Australia. However, the models do capture the negative trend over southern New Zealand, the strong negative trend in southern Chile (although this trend is broader than that in observations, extending both to the east coast and farther north, likely a result of varying resolution and orography among the models and multimodel averaging), and the positive trend across southeastern South America. When the analysis is extended over 1950–2005, 80% of the models agree on the decreasing trend across southern Chile.

As well as considering the MME trends, it is worth assessing the spread in modeled trends. Trends in regionally averaged land precipitation for individual models are assessed for three regions of observed precipitation decline: southeastern Africa, southeastern Australia, and the southern Chile region (these trends are shown in Fig. 4, discussed in section 3c). It is apparent that the majority of models do not reasonably simulate the observed trends across all three regions. In both southeastern Africa and southeastern Australia, only 16 out of 34 models simulate a negative trend in precipitation; in the southern Chile region 24 out of 34 models simulate a negative trend. In southeastern Australia, the region of strongest observed autumn precipitation decrease across the SH (Fig. 1a), no models simulate a precipitation decline greater than that observed; in fact, only one model (HadGEM2-ES) simulates a decline at least half as strong as that observed. In southeastern Africa, one model (IPSL-CM5A-MR) shows a stronger decline in precipitation than that observed, and three models (HadGEM2-CC,

HadGEM2-ES, and IPSL-CM5A-LR) show trends at least half as strong as that observed. In the southern Chile region, model representation is somewhat improved, with two models (GFDL-ESM2G and HadGEM2-CC) showing very similar trends to those observed, and five models (BNU-ESM, CCSM4, GFDL-ESM2M, GISS-E2-H, and INM-CM4) showing declines at least half as strong as observed. No model is able to capture the observed precipitation declines (simulating trends at least half as strong as those observed) in all three regions. HadGEM2-CC and HadGEM2-ES capture the precipitation decline in two regions each, although HadGEM2-CC also shows a strong precipitation increase in southeastern Australia, and HadGEM2-ES only shows a very weak precipitation decline in the southern Chile region. Based on the assessment of regional land precipitation trends, it is clear that no model is able to capture the hemispheric pattern of change. Consistent with findings drawn from trends in the MME, models have the most skill in simulating trends in the southern Chile region, and the least skill over southeastern Australia.

In summary, during autumn the CMIP5 models appear to have more skill in simulating past trends in the extratropical midlatitude regions than in the subtropical midlatitude regions. The ability of CMIP5 models to simulate historical trends over the latter part of the twentieth century in autumn precipitation seems largely unchanged compared to that of the CMIP3 models (not shown). MME trends over southern Africa seem somewhat less well represented in CMIP5 models, but there is a slight improvement in CMIP5 models, relative to CMIP3 models, over southeastern South America.

b. Observed and modeled SAM and HCE trends

To assess their influence on austral autumn precipitation, trends in the observed SH circulation indices and the models' representation of these must first be assessed. The spatial pattern of the first EOF of MSLP for each model is found to reasonably represent a SAM-like pattern when compared to the observations (not shown). The uncorrected NNR SAM pattern (i.e., the spatial pattern of the first EOF of NNR MSLP that has not been regressed onto the Marshall SAM index) accounts for ~39% of the variance, while the first EOF in the models accounts for between ~24% and 61% of the variance. Observed[2] and modeled SAM time series are

---

[2] Note that here we refer to the NNR SAM index; because both datasets are regressed onto the Marshall SAM index before EOF analysis, the observed 20CR SAM trend is very similar to the NNR SAM trend.

TABLE 1. CMIP5 models and simulations from the historical, RCP4.5 and RCP8.5 experiments used in this study.

Model	Modeling group	Country	Hist.	RCP4.5	RCP8.5
Australian Community Climate and Earth System Simulator version 1.0 (ACCESS1.0)	Commonwealth Scientific and Industrial Research Organization, and Bureau of Meteorology	Australia	y	y	y
Australian Community Climate and Earth System Simulator, version 1.3 (ACCESS1.3)	Commonwealth Scientific and Industrial Research Organization, and Bureau of Meteorology	Australia	y	y	y
Beijing Climate Center, Climate System Model, 1-1 (BCC-CSM1–1)	Beijing Climate Center, China Meteorological Administration	China	y	y	y
Beijing Normal University—Earth System Model (BNU-ESM)	College of Global Change and Earth System Science, Beijing Normal University	China	y		
Canadian Climate Model version 4 (CanCM4)	Canadian Centre for Climate Modeling and Analysis	Canada	y		
Canadian Earth System Model, version 2 (CanESM2)	Canadian Centre for Climate Modeling and Analysis	Canada	y	y	y
Community Climate System Model, version 4 (CCSM4)	National Center for Atmospheric Research	United States	y		
Community Earth System Model version 1, with Biogeochemistry (CESM1-BGC)	National Science Foundation, Department of Energy, National Center for Atmospheric Research	United States	y		
Community Earth System Model version 1, with Community Atmosphere Model, version 5 (CESM1-CAM5)	National Science Foundation, Department of Energy, National Center for Atmospheric Research	United States	y		
Community Earth System Model version 1, with Fast Chemistry (CESM1-FASTCHEM)	National Science Foundation, Department of Energy, National Center for Atmospheric Research	United States	y		
Centre National de Recherches Météorologiques Coupled Global Climate Model, version 5 (CNRM-CM5)	Centre National de Recherches Météorologiques, Centre Européen de Recherche et Formation Avancée en Calcul Scientifique	France	y	y	y
Commonwealth Scientific and Industrial Research Organisation Mark, version 3.6.0 (CSIRO-Mk3.6.0)	Commonwealth Scientific and Industrial Research Organization, and Queensland Climate Change Centre of Excellence	Australia	y	y	y
Flexible Global Ocean–Atmosphere–Land System Model gridpoint, version 2 (FGOALS-g2)	Institute of Atmospheric Physics, Chinese Academy of Sciences, and Tsinghua University	China	y		y
Flexible Global Ocean–Atmosphere–Land System Model gridpoint, second spectral version (FGOALS-s2)	Institute of Atmospheric Physics, Chinese Academy of Sciences	China	y		y
First Institute of Oceanography Earth System Model (FIO-ESM)	The First Institute of Oceanography, State Oceanic Administration	China			
Geophysical Fluid Dynamics Laboratory Climate Model, version 3 (GFDL-CM3)	National Oceanic and Atmospheric Administration Geophysical Fluid Dynamics Laboratory	United States	y*	y	y
Geophysical Fluid Dynamics Laboratory Earth Science Model 2G (GFDL-ESM2G)	National Oceanic and Atmospheric Administration Geophysical Fluid Dynamics Laboratory	United States	y		
Geophysical Fluid Dynamics Laboratory Earth Science Model 2M (GFDL-ESM2M)	National Oceanic and Atmospheric Administration Geophysical Fluid Dynamics Laboratory	United States	y		y
Goddard Institute for Space Studies Model E, coupled with the HYCOM ocean model (GISS-E2-H)	National Aeronautics and Space Administration Goddard Institute for Space Studies	United States	y		
Goddard Institute for Space Studies Model E, coupled with Russell ocean model (GISS-E2-R)	National Aeronautics and Space Administration Goddard Institute for Space Studies	United States	y	y	y

TABLE 1. (*Continued*)

Model	Modeling group	Country	Hist.	RCP4.5	RCP8.5
Third climate configuration of the Met Office Unified Model (HadCM3)	Met Office Hadley Centre	United Kingdom	y		
Hadley Centre Global Environmental Model 2, Carbon Cycle (HadGEM2-CC)	Met Office Hadley Centre	United Kingdom	y	y	y
Hadley Centre Global Environmental Model 2, Earth System (HadGEM2-ES)	Met Office Hadley Centre	United Kingdom	y		y
Institute of Numerical Mathematics Coupled Model, version 4.0 (INM-CM4)	Institute for Numerical Mathematics	Russia	y	y	y
L'Institut Pierre-Simon Laplace Coupled Model, version 5, coupled with NEMO, low resolution (IPSL-CM5A-LR)	Institut Pierre-Simon Laplace	France	y		y
L'Institut Pierre-Simon Laplace Coupled Model, version 5, coupled with NEMO, medium resolution (IPSL-CM5A-MR)	Institut Pierre-Simon Laplace	France	y	y	y
Model for Interdisciplinary Research on Climate, Earth System Model (MIROC-ESM)	Japan Agency for Marine-Earth Science and Technology, Atmosphere and Ocean Research Institute (The University of Tokyo), and National Institute for Environmental Studies	Japan	y	y	y
Model for Interdisciplinary Research on Climate, Earth System Model, Chemistry Coupled (MIROC-ESM-CHEM)	Japan Agency for Marine-Earth Science and Technology, Atmosphere and Ocean Research Institute (The University of Tokyo), and National Institute for Environmental Studies	Japan	y	y	y
Model for Interdisciplinary Research on Climate, version 4h (MIROC4h)	Atmosphere and Ocean Research Institute (The University of Tokyo), National Institute for Environmental Studies, and Japan Agency for Marine-Earth Science and Technology	Japan	y		
Model for Interdisciplinary Research on Climate, version 5 (MIROC5)	Atmosphere and Ocean Research Institute (The University of Tokyo), National Institute for Environmental Studies, and Japan Agency for Marine-Earth Science and Technology	Japan	y	y	Y
Max Planck Institute Earth System Model, low resolution (MPI-ESM-LR)	Max Planck Institute for Meteorology	Germany	y		
Meteorological Research Institute Coupled General Circulation Model, version 3 (MRI-CGCM3)	Meteorological Research Institute	Japan	y	y	y
Norwegian Earth System Model, intermediate resolution (NorESM1-M)	Norwegian Climate Centre	Norway	y	y	y
Norwegian Earth System Model, intermediate resolution with Carbon Cycle (NorESM1-ME)	Norwegian Climate Centre	Norway	y		

* Historical MSLP ends at 2004.

shown in Figs. 2a and 2b, respectively. Both SAM time series show a positive trend, although the trend in the MME is about half (53%) the magnitude of the observed NNR SAM trend. This agrees with previous findings using CMIP3 models, which also failed to simulate the strength of the observed positive SAM index trend during austral autumn (Fogt et al. 2009).

The spread of SAM trends simulated by the models can be seen in Fig. 2e: 27 out of 34 models simulate an increasing trend in the SAM index, although only 13 models simulate a trend at least half as strong as the corrected NNR SAM trend, and two of these models simulate trends that are much too strong compared to that observed (over twice the NNR trend; FGOALS-s2 and IPSL-CM5A-LR). Thus, out of the
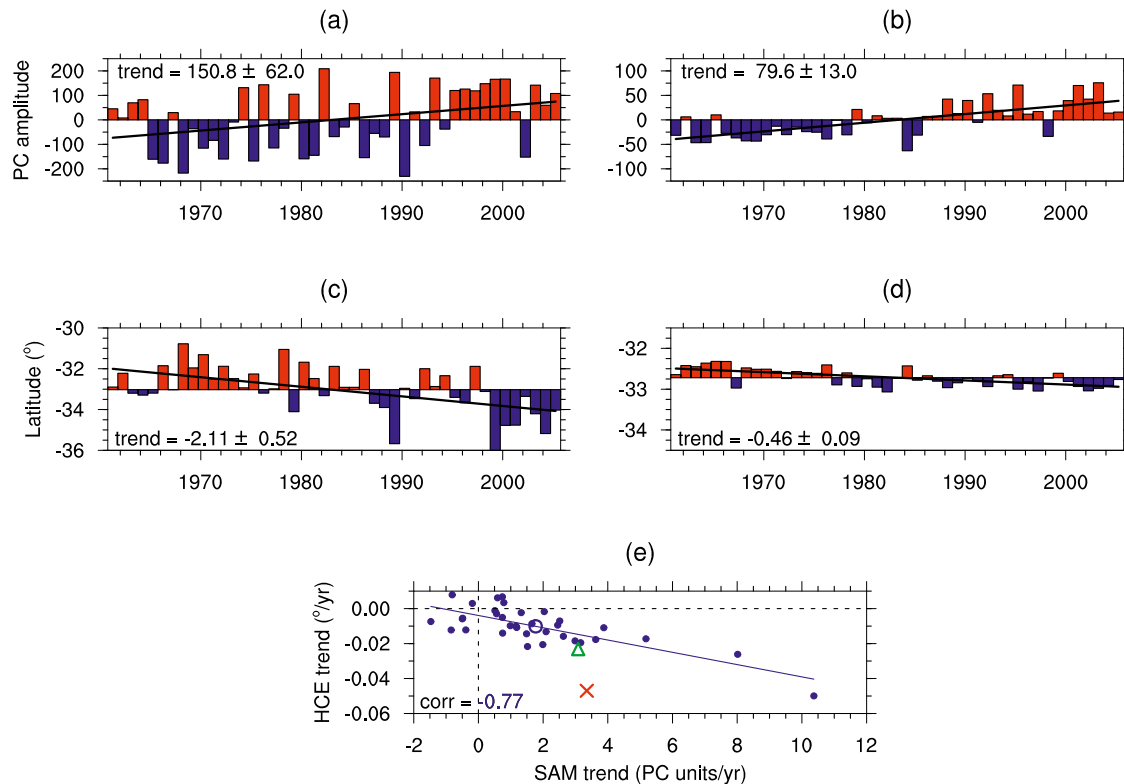
FIG. 2. Time series and trends of austral autumn (top) SAM and (middle) HCE over 1961–2005: (a),(c) NNR and (b),(d) CMIP5 historical MME. Note that the vertical scales in (a),(c) are twice those in (b),(d), respectively. In (a)–(d) a black line shows the linear trend and the trend value and standard error are indicated. (e) Trends in the HCE vs trends in the SAM for individual models (blue circles), the MME (large hollow blue circle), NNR (red cross), and 20CR (green triangle). The model line of best fit (blue line) and intermodel correlation coefficient are also shown. To calculate the observed SAM index both reanalyses are first corrected against the Marshall (2003) SAM index.

34 models analyzed here, 11 models generate SAM trends reasonably well (at least half the strength, and not exceeding twice the strength) compared to the observations.

The expansion of the subtropical dry zone as measured by HCE trends is shown for the reanalysis and CMIP5 models in Figs. 2c and 2d, respectively. The NNR expansion rate of ~2.1° per 45 years and the 20CR expansion rate of ~1.0° per 45 years are both slightly lower than trends reported elsewhere [e.g., ~2°–4.5° per 32 years over 1979–2010 in Cai et al. (2012)], likely because here the first portion of analysis is outside of the period of largest observed expansion. The weaker trend in the 20CR compared to the NNR agrees with previous findings (e.g., Stachnik and Schumacher 2011). The MME trend shows a poleward shift of 0.46° per 45 years, only ~22% of the magnitude of the NNR trend and ~46% of the magnitude of the 20CR trend. This is similar to previous studies of subtropical dry-zone expansion in CMIP3 models, which were found to significantly underestimate expansion rates compared to

observations (e.g., Johanson and Fu 2009; Son et al. 2009). Min and Son (2013) found a similar underestimation of HCE trends in CMIP5 models, with modeled trends during autumn in particular being weaker than reanalysis.

As for SAM trends, the spread among HCE trends as simulated by the models is depicted in Fig. 2e. For this metric, 29 out of 34 models simulate an expansion of the HCE. Only FGOALS-s2 (for which the simulated SAM trend is too strong compared to observations) simulates an expansion rate similar to that in NNR. However, 14 out of 34 models simulate a trend at least half as strong as that observed in 20CR. Of the 14 models that simulate a somewhat reasonable HCE expansion, seven of these also simulate reasonable SAM trends (CCSM4, CanESM2, GFDL-ESM2G, GISS-E2-H, GISS-E2-R, HadGEM2-CC, and IPSL-CM5A-MR).

Figure 2e also shows the relationship between the strength of simulated and observed trends in the HCE and the SAM. It is clear that there is a strong negative intermodel relationship among the models (correlation of −0.77, statistically significant at the 99% confidence
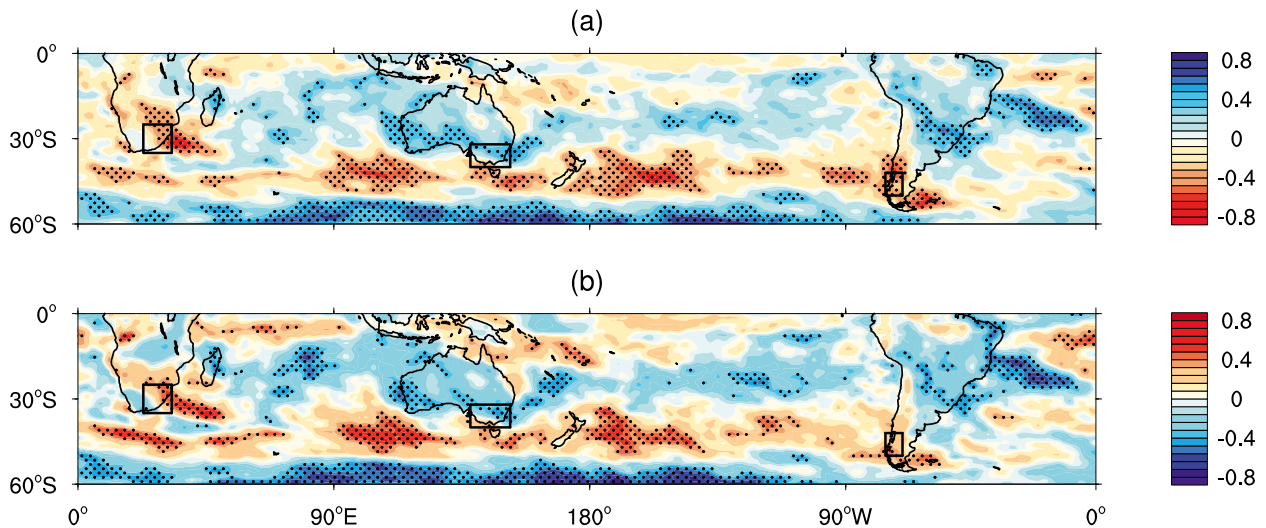
FIG. 3. Austral autumn intermodel correlation coefficients for the CMIP5 historical MME over 1961–2005, between precipitation trends and (a) SAM trends and (b) HCE trends. Stippling indicates where the correlation coefficients are significant at the 95% confidence level as determined by a two-sided Student's *t* test. Black boxes indicate the regions shown in Fig. 4.

level). This relationship is not surprising, given previous studies using CMIP3 models have shown linkage between these subtropical and extratropical modes of circulation (e.g., Previdi and Liepert 2007; Kang and Polvani 2011). Although not shown, the relationship among HCE trends, trends in the observed station-based SAM index of Marshall (2003), and the simulated SAM index calculated in the same manner (by interpolating modeled MSLP to station locations) yields the same conclusions: a strong negative relationship between the HCE and SAM trends persists, and the majority of models still underestimate the magnitude of the observed SAM trend. This provides confirmation that the underestimation of SAM trends by the models compared to the Marshall-corrected NNR SAM trend is not an artifact of spurious trends in the NNR, and that correcting the NNR against the Marshall SAM index allows the NNR to be used appropriately in such analysis.

c. Observed and modeled SAM and HCE interactions with precipitation

In regions of SAM influence, under the assumption that the spatial configuration of the SAM does not change so much over time so as to cause a response disconnection (e.g., Silvestri and Vera 2009), it may be expected that a greater SAM trend will be associated with a larger precipitation change. To test this hypothesis, Fig. 3a shows the intermodel relationship between precipitation trends and SAM trends during austral autumn. The SAM-signature dipole pattern over the Southern Ocean with a positive relationship (increased precipitation with a positive SAM trend) at 60°S and

a negative relationship at 45°S is prominent, with good model agreement. In these SAM-affected regions, the strength of modeled precipitation trends is closely linked to the strength of the SAM trends, with regions significant at the 95% confidence level indicated by stippling. The intermodel coherence is weaker farther north ~30°S, although a negative relationship over southeastern Africa and a positive relationship over much of southern Australia and southeastern South America are seen. Figure 3b shows the intermodel relationship between precipitation trends and HCE trends. In these panels the color bar has been reversed to account for the fact that subtropical dry-zone expansion is associated with a positive SAM trend. Relationships are similar to Fig. 3a, as expected, given the strong correlation between modeled trends of the HCE and SAM as seen in Fig. 2e.

Figure 4 provides further insight into the intermodel spread between trends in precipitation and trends in the SAM and HCE. In this figure, precipitation is averaged over southeastern Africa, southeastern Australia, and the southern Chile region. Note that the regions selected for this figure are based on those with the strongest observed precipitation declines (Fig. 1a). Figure 4 reinforces the conclusions drawn from Fig. 3: that the intermodel relation between precipitation trends and trends in the SAM and HCE are strongest in the extratropics (~45°S) and weaker farther equatorward (~30°S).

Expanding upon the relationship between the SAM and precipitation in the models, a combination of the influences of interannual variability and trends of the SAM on precipitation during austral autumn is also
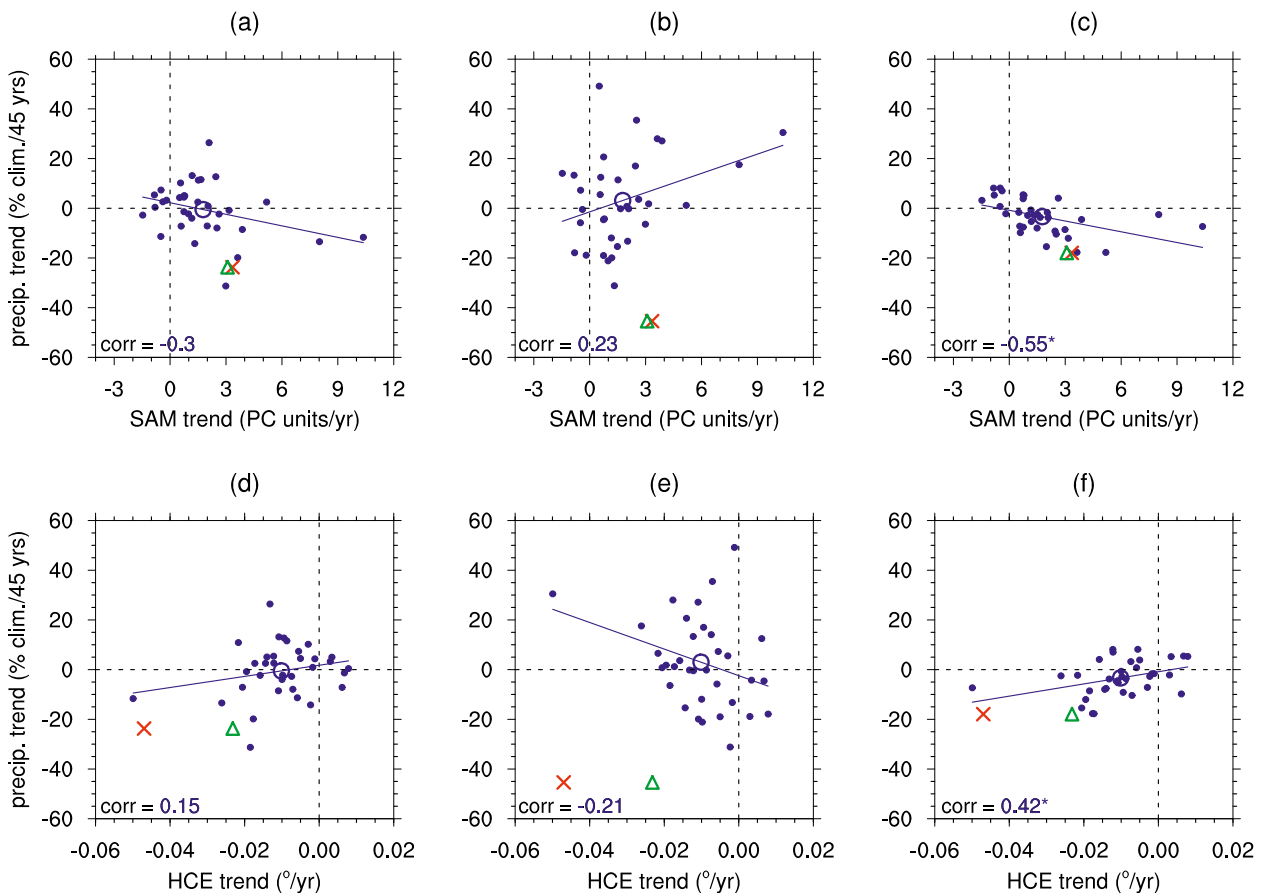
FIG. 4. Relationships over 1961–2005 between simulated austral autumn regional land precipitation trends and (a)–(c) SAM trends and (d)–(f) HCE trends. Regional land precipitation trends are averaged over southeastern Africa (25°–35°S, 23°–33°E), southeastern Australia (32°–40°S, 138°–152°E), and the southern Chile region (42°–50°S, 70°–76°W), as shown by the boxes in Fig. 3. These regions are selected based on regions of observed precipitation decline (Fig. 1a) of comparable size. Each panel shows trends in individual models (blue circles), the MME (hollow blue circle), NNR (red cross), and 20CR (green triangle). The model line of best fit (blue line) and intermodel correlation coefficient are also shown. Correlation coefficients are statistically significant as determined by a two-sided Student's t test in (c) at the 99% level and (f) at the 95% level indicated by an asterisk (*).

investigated, with Figs. 5a and 5b showing precipitation trends congruent with trends in the SAM [refer to Eq. (4)] for the observations and models, respectively. The patterns of the trends in the observations and in the MME are similar, although trends in the MME are weaker as a consequence of the weaker SAM trends present in the models (cf. Figs. 2a and 2b). As expected based on the SAM's influence, the modeled trends are largely zonal, with a broad pattern of weak precipitation increase across the high latitudes (~60°S), reduced precipitation across the midlatitudes (~45°S), and increased precipitation in the subtropics (~30°S). A strong negative MME trend is seen over southern Chile: in the observations this trend is a result of a poleward shift in storm tracks (Haylock et al. 2006). Weak positive MME trends over southern Africa and southern Australia are also seen. Observational analysis has shown the positive

phase of the SAM during austral spring and summer to be associated with increased precipitation in southeastern Australia as a result of increased convection in the Tasman Sea region and moisture-laden anomalous easterly flow impinging on the east coast (Hendon et al. 2007). However, little relationship between the SAM and autumn precipitation in the observations is seen, both in this study (Fig. 5a) and in previous analysis (Hendon et al. 2007), differing from the MME (Fig. 5b).

Comparing Figs. 5a and 5b, the models fail to capture the two regions that exhibit weak precipitation declines, ~20°S in western Africa and northeastern Australia, and the SAM-congruent drying trend in southeastern South America (a region of observed rainfall increase). This latter disagreement between observations and models was also noted in the annual relationship of precipitation and the SAM in CMIP3 models (see Figs. 2e and 2f
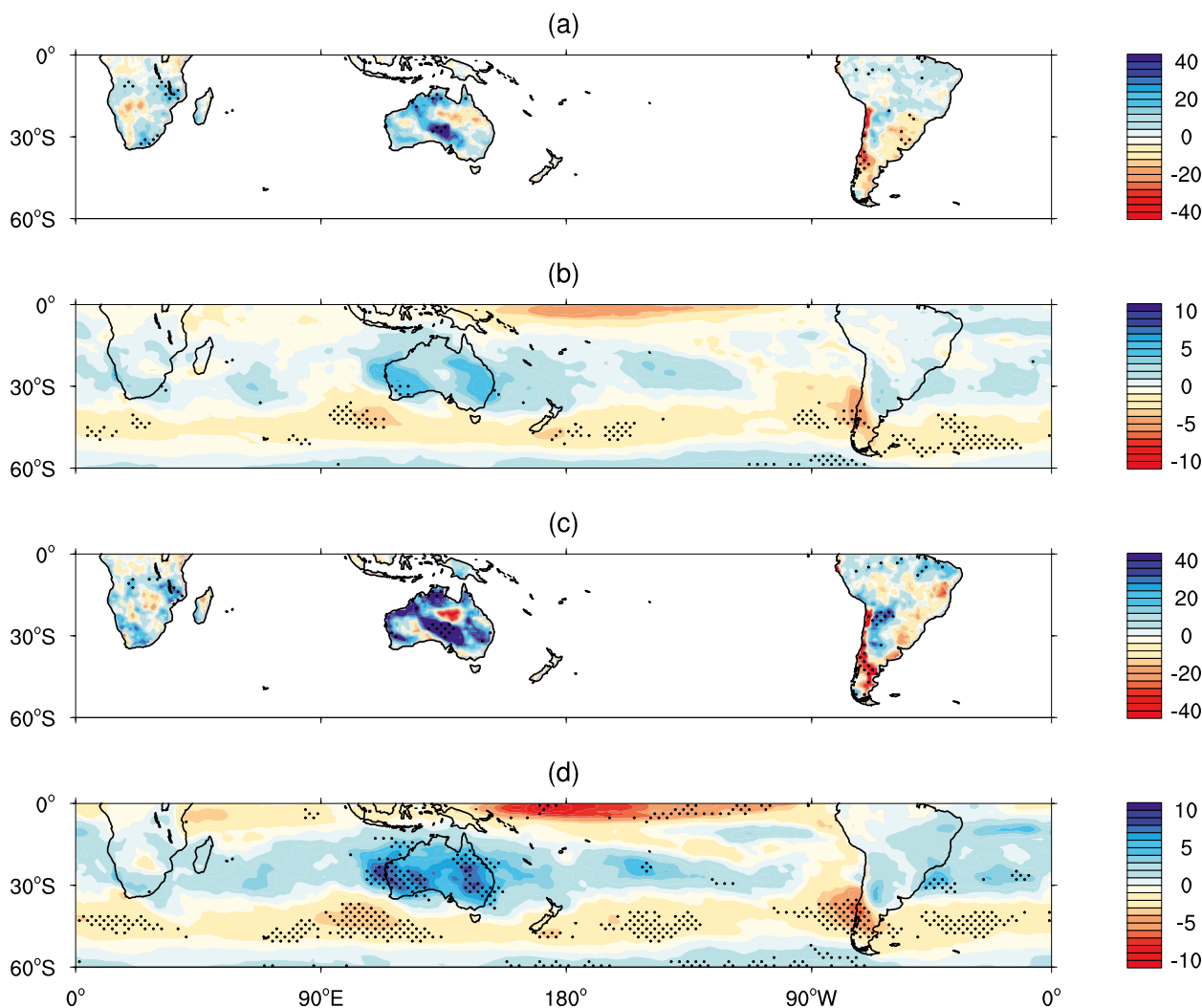
FIG. 5. Austral autumn trends in precipitation congruent with trends in the SAM and HCE over 1961–2005: (a),(c) observations and (b),(d) CMIP5 historical MME. Trends are expressed as a percentage change of climatology per 45 years and note that the color bars have different limits. Stippling in (a),(c) indicates where the regression coefficient between the SAM–HCE and precipitation is significant at the 95% confidence level as determined by a two-sided Student's *t* test and in (b),(d) where ≥80% of the 34 models agree on the sign of the ensemble-mean trend.

in Karpechko et al. 2009). Silvestri and Vera (2003) noted that the rainfall response to the SAM in this region is present in autumn and spring and is caused by the positive SAM-induced maintenance of an anomalous anticyclone over the region, which reduces cyclonic activity and thus precipitation. Karpechko et al. (2009) thus suggested that this mechanism may be missing in the CMIP3 models. Based on these results, this also appears to be the case for the CMIP5 models. Furthermore, Silvestri and Vera (2009) suggest that during austral spring, the relationship between the SAM and precipitation in southeastern South America may vary on decadal time scales, as the relationship is found to depend on the period of analysis. This suggests the SAM-precipitation response in this region has strong

temporal variability, and if a similar nonstationarity exists in austral autumn, it may contribute to the models poor simulation of the response here.

Precipitation trends congruent with HCE trends are shown in Figs. 5c and 5d. In both the observations and MME, there is a very strong similarity to the corresponding SAM-congruent precipitation trends (cf. Figs. 5a and 5b). This suggests that within CMIP5 models, it is not just the relationship between the strength of precipitation trends and the strength of the trends in both the SAM and HCE that are similar, but also the relationship between precipitation variability with both SAM and HCE variability. This finding is consistent with analysis of CMIP3 models, which exhibit strong relationships between SAM and HCE interannual

variability during austral summer (Kang and Polvani 2011). The notable exception in the MME HCE-congruent precipitation trends (compared to the SAM-congruent precipitation trends) is the stronger and more significant relationship over Australia. The reason for the greater coherence in this region is unknown. Cai et al. (2012) found a stronger coherence between the HCE and rainfall over Australia than in other SH landmass regions; however, they also found the sub-tropical dry-zone expansion to be linked with the observed April–May rainfall decline in southeastern Australia. Here, results suggest the subtropical dry-zone expansion should have led to increased precipitation over southeastern Australia. These seemingly conflict-ing results may be a result of the different time periods and/or seasons analyzed [Cai et al. (2012) analyzed April–May over 1948–2010] or climatological biases in the models.

Comparing Figs. 5a and 5c with Fig. 1a, it appears that the observed austral autumn subtropical dry-zone ex-pansion and positive SAM trend may have contributed to the observed precipitation decrease in southern Chile, as well as potentially offsetting the observed drying across southeastern Africa and southeastern Australia. Likewise, comparing Figs. 5b and 5d with Fig. 1b, it appears that the modeled subtropical dry-zone ex-pansion and positive SAM trend may have accounted for the MME precipitation decreases in southern mid-latitude regions (e.g., southern New Zealand and southern Chile). That the modeled trends in circulation indices are much weaker than observed may have con-tributed to the MME precipitation trends also being weaker than observed. However, Cai et al. (2012) have recently suggested that in southern Chile the observed April–May precipitation reduction cannot be explained by the subtropical dry-zone expansion; this reflects the fact that the observed zonally averaged HCE has shifted poleward in recent decades, while the region of impact of the HCE on precipitation and MSLP in the vicinity of southern Chile has shifted equatorward (Cai et al. 2012). As emphasized above for southeastern Australia (and also applicable for southern Chile), these seemingly conflicting findings may be a result of the different time periods and/or seasons analyzed. This suggests that such results are sensitive to seasonal definitions and de-cadal variability, such as the Pacific decadal oscilla-tion, which has recently been shown to influence SAM and HCE variability in austral summer (Wang and Cai 2013). However, the MME results imply that re-moving the influence of multidecadal variability (through multimodel averaging), an impact from the subtropical dry-zone expansion can be manifested in southern Chile.

Considering the intermodel spread (not shown) in SAM- (HCE)-congruent precipitation trends over south-eastern Africa, southeastern Australia and the southern Chile region, not surprisingly, models that simulate reasonably strong SAM (HCE) trends also tend to sim-ulate stronger SAM- (HCE)-congruent precipitation trends. CanESM2 and GFDL-ESM2, which simulate trends in both the SAM and HCE well, are the only models besides FGOALS-s2 (which simulates an overly strong SAM trend) to also capture the strength of the congruent precipitation trends in all three regions rea-sonably well. However, there is an overall improvement in the number of models able to simulate congruent precipitation trends in the same direction as that ob-served, compared to precipitation trends alone. For south-eastern Africa, southeastern Australia, and the southern Chile region, 23 (28), 24 (29), and 26 (30) models re-spectively simulate a SAM- (HCE)-congruent precipi-tation trend of the observed sign.

d. Future SAM and HCE interactions with precipitation

In the first half of the twenty-first century, increasing concentrations of greenhouse gases are expected to continue to contribute to the positive trend in the SAM in all seasons, although recovery of stratospheric ozone is expected to force a negative trend in the tropospheric SAM during austral summer (Shindell and Schmidt 2004; Perlwitz et al. 2008; McLandress et al. 2011). Further expansion of the subtropical dry zone is also anticipated as atmospheric greenhouse gas concentra-tions increase (e.g., Seidel et al. 2008).

The modeled trends in the SAM and HCE during austral autumn over 2006–50 are shown in Fig. 6a (RCP4.5 in blue, RCP8.5 in red). As expected, the MMEs for both experiments show a continuation of the positive trend in the SAM and subtropical dry-zone expansion, with stronger trends for both metrics in the RCP8.5 MME, although there is considerable overlap between modeled trends for the two experiments. As with the historical experiment, there is a strong inter-model coherence between the strength of SAM and HCE trends: within the RCP4.5 experiment the inter-model correlation is -0.63, within the RCP8.5 experi-ment the intermodel correlation is -0.64, and across both sets of experiments the intermodel correlation is -0.63 (significance for all cases exceeding the 99% level). The effects of these trends on midlatitude pre-cipitation trends in future projections thus need to be assessed.

Figures 6b and 6c show the MME-projected twenty-first-century precipitation trends for the two RCP ex-periments. The large-scale patterns of change are similar
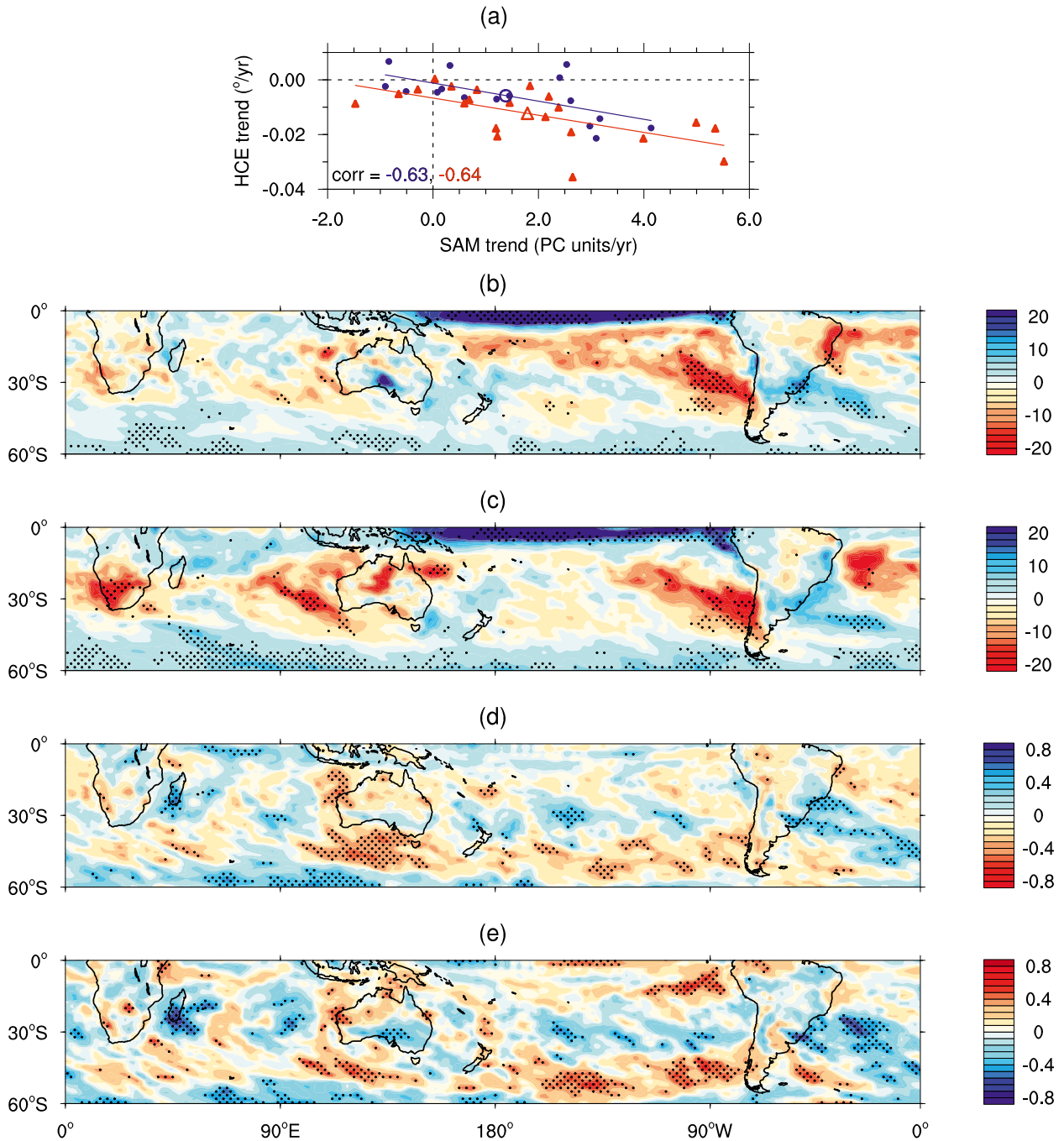
(a)

(b)

(c)

(d)

(e)

FIG. 6. Future austral autumn projections from the RCP4.5 and RCP8.5 experiments over 2006–50: (a) trends in the HCE vs trends in the SAM for RCP4.5 models (blue circles), RCP8.5 models (red triangles), and the MMEs (hollow blue circle and red triangle). The lines of best fit and intermodel correlations are also shown. (b) RCP4.5 and (c) RCP8.5 MME trends in precipitation, expressed as a percentage change of climatology per 45 years, with stippling indicating where ≥80% of the 16 and 21 models, respectively, agree on the sign of the ensemble-mean trend. Combined RCP4.5 and RCP8.5 intermodel correlation coefficients of precipitation trends vs (d) SAM trends and (e) HCE trends, with stippling indicating where the correlation coefficients are significant at the 95% confidence level, as determined by a two-sided Student's t test.

across the two experiments: an increase in precipitation is seen across the Southern Ocean, decreasing trends are seen over southern Africa and over the eastern Pacific extending over southern Chile, and an increasing trend is seen in southeastern South America. In general, trends are slightly stronger in the RCP8.5 MME, with the greatest change over southern Africa (~15%–20%). However, a reversal of trends occurs over southern

Australia when comparing the RCP4.5 MME (increase in precipitation) to the RCP8.5 MME (reduction in precipitation). For southern Africa and southern Chile, the models show a stronger consensus that in the near future precipitation is likely to continue to decline; however, for southern Australia the direction of future precipitation trends is uncertain. This suggests that unforced climate variability may dominate such changes, at least up to 2050.

The intermodel correlations between the strength of precipitation trends and trends in the SAM and HCE are shown in Figs. 6d and 6e, respectively. Despite the continuation of SAM and HCE trends in the same direction as in the historical experiment, the intermodel relationships are less coherent than the corresponding historical experiment correlations (Fig. 3). For both the strength of SAM and HCE trends, projected relationships with precipitation trends are less zonally oriented, although a positive (negative) relationship between SAM (HCE) trends and precipitation trends is seen at high latitudes over the Southern Ocean and a statistically significant negative (positive) relationship at midlatitudes (~45°S), extending from south of Australia across the Pacific to southern Chile. This supports findings from analysis of the historical experiment: precipitation trends in southern Chile are strongly affected by the strength of trends in both the SAM and subtropical dry-zone expansion, which are in turn forced by anthropogenic climate change. Thus, future emissions could have a large impact on austral autumn precipitation in southern Chile.

Results for southern Africa and southern Australia are less conclusive. In southern Africa, the strength of precipitation trends in the western part of this region show a negative (positive) relationship with the strength of SAM (HCE) trends. Although these relationships are fairly localized, they suggest that part of this region, like southern Chile, may experience impacts on precipitation dependent on the strength of anthropogenic forcing. Relationships are essentially absent in southeastern Africa, suggesting that the SAM and subtropical dry-zone expansion may have little impact in this region in the future.

Over southern Australia, relationships with a positive trending SAM suggest decreasing precipitation at the very southern edge of the continent, a thin band of increasing precipitation farther north, and decreasing precipitation north of 30°S, although the relationships are not statistically significant. This increasing precipitation is more obvious in the relationship with the subtropical dry-zone expansion, which suggests increasing precipitation over the entire southeastern portion with a stronger expansion of the subtropical dry zone. Since precipitation trends over southern Australia vary between RCP

scenarios, and the SAM and HCE influences are most varied in this region, this suggests that future trends in austral autumn precipitation in this region are uncertain. CMIP3 models have been shown to have a poor representation of key southeastern Australian rainfall processes such as cutoff lows and atmospheric blocking (Grose et al. 2012). Detailed analysis of such deficiencies in CMIP5 models is beyond the scope of this study, but incorrect rainfall generation mechanisms may contribute to the questionable projections of precipitation for the region.

Future precipitation trends congruent with SAM and HCE trends are not shown here: spatial patterns are very similar to those seen in the historical experiment (Figs. 5b and 5d), with the strength of precipitation trends increasing for the RCP8.5 experiment, where SAM and HCE trends are stronger. Such results suggest the interannual relationship between precipitation and both the SAM and HCE remain similar in the future scenarios.

4. Conclusions

The ability of CMIP5 models to capture the observed trends in austral autumn precipitation across SH midlatitude regions is investigated. The SH subtropical dry-zone expansion and trends in the SAM as simulated by the models are also assessed. On the whole, CMIP5 models are unable to capture many of the observed trends in precipitation during autumn, notably failing to simulate observed declines in southern Africa and southeastern Australia. Trends in extratropical regions such as southern Chile are better simulated. The majority of models simulate positive trends in the SAM (27 out of 34 models) and subtropical dry-zone expansion (29 out of 34 models). The positive trend in the MME SAM index is only about half the strength of that observed, although 11 models are considered to simulate the SAM trend reasonably well. The large range in the subtropical dry-zone expansion rates estimated from NNR and 20CR makes assessment of the models' performance difficult.

Nevertheless, regions where austral autumn precipitation trends are simulated more accurately tend to correspond to regions strongly influenced by the SAM, with precipitation trends found to be congruent with SAM trends in both the models and the observations, in agreement with previous studies (e.g., using CMIP3 models; Karpechko et al. 2009). The strength of modeled precipitation trends in these regions is also found to be proportional to the strength of the modeled SAM trends. A strong coherence between the strength of SAM and HCE trends in the models is noted and regions

of strong SAM influence tend to also be strongly influenced by subtropical dry-zone expansion.

As the subtropical dry-zone expansion and positive SAM trend are projected to continue in the first half of the twenty-first century, it is likely that the autumn decline in precipitation in extratropical midlatitude regions will also continue. The strength of the future MME precipitation trends in midlatitude regions is found to be proportional to the strength of the modeled trends in the SAM and HCE. Thus, results suggest that unabated greenhouse gas–induced climate change will have a large impact on precipitation in regions under the influence of the SAM and subtropical dry-zone expansion, such as southern Chile. Future trends during austral autumn in southern Australia are less clear and the autumn SAM trend and subtropical dry-zone expansion cannot account for them, and in fact may have offset other climate variability modes that have contributed to the observed precipitation decline. To assist in reducing the uncertainty in future precipitation projections, further work investigating the limited ability of climate models in simulating observed historical trends in precipitation over many SH regions is required.

REFERENCES

Adler, R. F., and Coauthors, 2003: The Version-2 Global Precipitation Climatology Project (GPCP) monthly precipitation analysis (1979–present). *J. Hydrometeor.,* **4,** 1147–1167.

Arblaster, J., and G. Meehl, 2006: Contributions of external forcings to southern annular mode trends. *J. Climate,* **19,** 2896–2905.

Beck, C., J. Grieser, and B. Rudolf, 2005: A new monthly precipitation climatology for the global land areas for the period 1951 to 2000. DWD, Climate Status Report 2004, 181–190.

Cai, W., and T. Cowan, 2007: Trends in Southern Hemisphere circulation in IPCC AR4 models over 1950–99: Ozone depletion versus greenhouse forcing. *J. Climate,* **20,** 681–693.

——, and ——, 2008a: Dynamics of late autumn rainfall reduction over southeastern Australia. *Geophys. Res. Lett.,* **35,** L09708, doi:10.1029/2008GL033727.

——, and ——, 2008b: Evidence of impacts from rising temperature on inflows to the Murray-Darling basin. *Geophys. Res. Lett.,* **35,** L07701, doi:10.1029/2008GL033390.

——, and ——, 2013: Southeast Australia autumn rainfall reduction: A climate-change-induced poleward shift of ocean–atmosphere circulation. *J. Climate,* **26,** 189–205.

——, P. van Rensch, S. Borlace, and T. Cowan, 2011: Does the southern annular mode contribute to the persistence of the multidecade-long drought over southwest Western Australia? *Geophys. Res. Lett.,* **38,** L14712, doi:10.1029/2011GL047943.

——, T. Cowan, and M. Thatcher, 2012: Rainfall reductions over Southern Hemisphere semi-arid regions: The role of subtropical dry zone expansion. *Sci. Rep.,* **2,** 702, doi:10.1038/srep00702.

Compo, G., and Coauthors, 2011: The Twentieth Century Reanalysis Project. *Quart. J. Roy. Meteor. Soc.,* **137,** 1–28, doi:10.1002/qj.776.

Drosdowsky, W., 2005: The latitude of the subtropical ridge over eastern Australia: The L index revisited. *Int. J. Climatol.,* **25,** 1291–1299, doi:10.1002/joc.1196.

Fogt, R. L., J. Perlwitz, A. J. Monaghan, D. H. Bromwich, J. M. Jones, and G. J. Marshall, 2009: Historical SAM variability. Part II: Twentieth-century variability and trends from reconstructions, observations, and the IPCC AR4 models. *J. Climate,* **22,** 5346–5365.

Frederiksen, J. S., and C. S. Frederiksen, 2007: Interdecadal changes in Southern Hemisphere winter storm track modes. *Tellus,* **59A,** 559–617.

Fyfe, J., 2003: Extratropical Southern Hemisphere cyclones: Harbingers of climate change. *J. Climate,* **16,** 2802–2805.

Gillett, N., T. Kell, and P. Jones, 2006: Regional climate impacts of the southern annular mode. *Geophys. Res. Lett.,* **33,** L23704, doi:10.1029/2006GL027721.

Gong, D., and S. Wang, 1999: Definition of Antarctic Oscillation index. *Geophys. Res. Lett.,* **26,** 459–462, doi:10.1029/1999GL900003.

Grose, M., M. Pook, P. McIntosh, J. Risbey, and N. Bindoff, 2012: The simulation of cutoff lows in a regional climate model: Reliability and future trends. *Climate Dyn.,* **39,** 445–459, doi:10.1007/s00382-012-1368-2.

Gruber, A., X. Su, M. Kanamitsu, and J. Schemm, 2000: The comparison of two merged rain gauge–satellite precipitation datasets. *Bull. Amer. Meteor. Soc.,* **81,** 2631–2644.

Haylock, M. R., and Coauthors, 2006: Trends in total and extreme South American rainfall in 1960–2000 and links with sea surface temperature. *J. Climate,* **19,** 1490–1512.

Hendon, H. H., D. W. J. Thompson, and M. C. Wheeler, 2007: Australian rainfall and surface temperature variations associated with the Southern Hemisphere annular mode. *J. Climate,* **20,** 2452–2467.

Hu, Y., and Q. Fu, 2007: Observed poleward expansion of the Hadley circulation since 1979. *Atmos. Chem. Phys.,* **7,** 5229–5236.

——, C. Zhou, and J. Liu, 2011: Observational evidence for poleward expansion of the Hadley circulation. *Adv. Atmos. Sci.,* **28,** 33–44.

Johanson, C. M., and Q. Fu, 2009: Hadley cell widening: Model simulations versus observations. *J. Climate,* **22,** 2713–2725.

Kalnay, E., and Coauthors, 1996: The NCEP/NCAR 40-Year Reanalysis Project. *Bull. Amer. Meteor. Soc.,* **77,** 437–471.

Kang, S., and L. Polvani, 2011: The interannual relationship between the latitude of the eddy-driven jet and the edge of the Hadley cell. *J. Climate,* **24,** 563–568.

Karpechko, A. Y., N. P. Gillett, G. J. Marshall, and J. A. Screen, 2009: Climate impacts of the southern annular mode simulated by the CMIP3 models. *J. Climate,* **22,** 3751–3768.

Kidston, J., J. Renwick, and J. McGregor, 2009: Hemispheric-scale seasonality of the southern annular mode and impacts on the climate of New Zealand. *J. Climate,* **22,** 4759–4770.

Marshall, G., 2003: Trends in the southern annular mode from observations and reanalyses. *J. Climate,* **16,** 4134–4143.

McLandress, C., T. Shepherd, J. Scinocca, D. Plummer, M. Sigmond, A. Jonsson, and M. Reader, 2011: Separating the dynamical effects of climate change and ozone depletion. Part II: Southern Hemisphere troposphere. *J. Climate,* **24,** 1850–1868.

Meneghini, B., I. Simmonds, and I. N. Smith, 2008: Association between Australian rainfall and the southern annular mode. *Int. J. Climatol.,* **27,** 109–121.

Miller, R. L., G. A. Schmidt, and D. T. Shindell, 2006: Forced annular variations in the 20th century Intergovernmental Panel on Climate Change Fourth Assessment Report models. *J. Geophys. Res.,* **111,** D18101, doi:10.1029/2005JD006323.

Min, S.-K., and S.-W. Son, 2013: Multimodel attribution of the Southern Hemisphere Hadley cell widening: Major role of ozone depletion. *J. Geophys. Res.,* **118,** 3007–3015, doi:10.1002/jgrd.50232.

Murphy, B. F., and B. Timbal, 2008: A review of recent climate variability and climate change in southeastern Australia. *Int. J. Climatol.,* **28,** 859–879.

Nicholls, N., 2010: Local and remote causes of the southern Australian autumn–winter rainfall decline, 1958–2007. *Climate Dyn.,* **34,** 835–845, doi:10.1007/s00382-009-0527-6.

Perlwitz, J., S. Pawson, R. Fogt, J. Nielson, and W. Neff, 2008: Impact of stratospheric ozone hole recovery on Antarctic climate. *Geophys. Res. Lett.,* **35,** L08714, doi:10.1029/2008GL033317.

Polvani, L., D. Waugh, G. Correa, and S.-W. Son, 2011: Stratospheric ozone depletion: The main driver of twentieth-century atmospheric circulation changes in the Southern Hemisphere. *J. Climate,* **24,** 795–812.

Previdi, M., and B. G. Liepert, 2007: Annular modes and Hadley cell expansion under global warming. *Geophys. Res. Lett.,* **34,** L22701, doi:10.1029/2007GL031243.

Purdie, H., A. Mackintosh, W. Lawson, B. Anderson, U. Morgenstern, T. Chinn, and P. Mayewski, 2011: Interannual variability in net accumulation on Tasman Glacier and its relationship with climate. *Global Planet. Change,* **77,** 142–152.

Reason, C. J. C., and M. Rouault, 2005: Links between the Antarctic Oscillation and winter rainfall over western South Africa. *Geophys. Res. Lett.,* **32,** L07705, doi:10.1029/2005GL022419.

Risbey, J., M. Pook, P. McIntosh, M. Wheeler, and H. Hendon, 2009: On the remote drivers of rainfall variability in Australia. *Mon. Wea. Rev.,* **137,** 3233–3253.

Seidel, D., Q. Fu, W. Randall, and T. Reichler, 2008: Widening of the tropical belt in a changing climate. *Nat. Geosci.,* **1,** 21–24, doi:10.1038/ngeo.2007.38.

Shindell, D., and G. Schmidt, 2004: Southern Hemisphere climate responses to ozone changes and greenhouse gas increases. *Geophys. Res. Lett.,* **31,** L18209, doi:10.1029/2004GL020724.

Silvestri, G. E., and C. S. Vera, 2003: Antarctic Oscillation signal on precipitation anomalies over southeastern South America. *Geophys. Res. Lett.,* **30,** 2115, doi:10.1029/2003GL018277.

——, and ——, 2009: Nonstationary impacts on the southern annular mode on Southern Hemisphere climate. *J. Climate,* **22,** 6142–6148.

Son, S.-W., N. Tandon, M. Lorenzo, and D. Waugh, 2009: Ozone hole and Southern Hemisphere climate change. *Geophys. Res. Lett.,* **36,** L15705, doi:10.1029/2009GL038671.

——, and Coauthors, 2010: Impact of stratospheric ozone on Southern Hemisphere circulation change: A multimodel assessment. *J. Geophys. Res.,* **115,** D00M07, doi:10.1029/2010JD014271.

Stachnik, J., and C. Schumacher, 2011: A comparison of the Hadley circulation in modern reanalyses. *J. Geophys. Res.,* **116,** D22102, doi:10.1029/2011JD016677.

Taylor, K. E., R. J. Stouffer, and G. A. Meehl, 2012: An overview of CMIP5 and the experiment design. *Bull. Amer. Meteor. Soc.,* **93,** 485–498.

Thompson, D. W. J., and S. Solomon, 2002: Interpretation of recent Southern Hemisphere climate change. *Science,* **296,** 895–899.

——, and J. M. Wallace, 2000: Annular modes in the extratropical circulation. Part I: Month-to-month variability. *J. Climate,* **13,** 1000–1016.

Timbal, B., and W. Drosdowsky, 2013: The relationship between the decline of southeastern Australian rainfall and the strengthening of the subtropical ridge. *Int. J. Climatol.,* **33,** 1021–1034, doi:10.1002/joc.3492.

Wang, G., and W. Cai, 2013: Climate change impact on the 20th-century relationship between the southern annular mode and global mean temperature. *Sci. Rep.,* **3,** 2039, doi:10.1038/srep02039.

Xie, P., and P. Arkin, 1997: Global precipitation: A 17-year monthly analysis based on gauge observations, satellite estimates, and numerical model outputs. *Bull. Amer. Meteor. Soc.,* **78,** 2539–2588.

Yin, J. H., 2005: A consistent poleward shift of the storm tracks in simulations of 21st century climate. *Geophys. Res. Lett.,* **32,** L18701, doi:10.1029/2005GL023684.

Zhou, T., R. Yu, H. Li, and B. Wang, 2008: Ocean forcing to changes in global monsoon precipitation over the recent half-century. *J. Climate,* **21,** 3833–3852.